

# Controlling the Roughening of Growing Electrochemical Interfaces using Temperature Gradients

Asghar Aryanfar <sup>\*†§</sup>, Ali Tayyar<sup>‡</sup>, William A. Goddard III<sup>§</sup>

<sup>†</sup> *Boğaziçi University <sup>1</sup>, Bebek, Istanbul, Turkey 34342*

<sup>‡</sup> *American University of Beirut, Riad El Solh, Beirut, Lebanon 1107 2020*

<sup>§</sup> *California Institute of Technology, 1200 E California Blvd, Pasadena, CA 91125*

The excessive dendritic development during the electrochemical evolution of the microstructures in rechargeable batteries can ultimately cause a short circuit, thermal instability/runaway, and loss of active material. We initially develop a computational framework to quantify the bias of the electrodeposition on the roughened interface favoring the convex zones. Subsequently, we impose a countering temperature effect to enhance the diffusion on the trailing concave zones. Consequently, we establish a stability criterion for controlling surface roughening where the visualized space of parameters establishes a relationship between the geometry of the interface, the physical properties of the electrolyte, and the charging conditions. The developed framework could be useful for controlling the propagation of the microstructures and the prevention of runaway, during prolonged cycles, particularly when the surface roughness gets pronounced in the later stage of cycle life.

**Keywords:** Rough interface, stabilizing, electric field, temperature gradients, curvature effect.

## 1 Introduction

The increasing necessity for energy in the past years has required the innovation of higher-energy density energy storage systems with enhanced performance [1]. Among many technological innovations, batteries

---

<sup>\*</sup>Corresponding author, Email: [aryanfar@caltech.edu](mailto:aryanfar@caltech.edu)

<sup>1</sup>a.k.a Bosphorus University.

have shown great potential as a clean source of electrical energy. More recently, lithium-ion batteries (LIBs) have been widely used in portable electronics, manufacturing, and electric cars/scooters industry [2, 3] as well as the green energy sector [4, 5], which exceeds billions of units manufactured throughout the world [6].

In a more specific way, lithium-ion batteries (LIBs) have been widely investigated, due to lithium’s extremely high theoretical specific capacity ( $3860mAhg^{-1}$ ), low density ( $0.59gcm^{-3}$ ), the lowest negative electrochemical potential ( $-3.04V$  vs. the standard hydrogen electrode)[7], and design flexibility [8]. In this regard, the growth of dendrites, a tree-like microstructure induced by the expansion of conductive filaments on the lithium electrode has been a critical issue since they grow with extreme porosity, leading to excessive reach and causing short-circuit [9, 10]. As well, it may detach from the thinner part of the branches during the dissolution (i.e. discharge), and create the so-called “dead lithium”[11], causing thermal instability [12, 13] and capacity decay [14, 15].

The precise process of dendritic growth remains not entirely grasped, yet it is generally recognized to be impacted by several factors such as current density [16, 17, 18], electrolyte composition [12, 19, 20], solid electrolyte interphase (*SEI*) [21, 22], and surface defects (i.e. kinks) [23]. The physical characterizations comprise porosity [24], tortuosity [25], and MacMullin Number [26], the geometry and micro-scale curvature [27, 28], and the sand time effect on growth transition [29].

The developed models include coupling the electrochemical potential to the stress and the formation of micro-cracks [30, 31], phase-field modeling [32, 33, 34], diffusion-limited aggregation [35], coarse-grained modeling [36, 37], smoothed particle hydrodynamics [38, 39], and sharp interface modeling [40, 41].

Several engineering ideas have tried to control the dendritic propagation, including shielding techniques [42], imposing external magnetic fields[43], guiding scaffolds [44], using nano-fiber arrays in the polymer electrolyte [45], applying prestress to stabilize planar growth and reduce surface roughening, [46], and using an-isotropic electrolytes to controlling electric-field gradients offering potential strategies to improve battery stability and potentially suppressing dendrite formation [47]. Additionally, they have ascribed that the growth rate could be controlled when lowering the charge transfer coefficients [48], applying forced advection and cross-flow [49, 50]. It could get stabilized under elastic prestress [46], the higher surface roughness and thinner SEI layer could exacerbate the dendritic propagation [51, 52, 53], and described the kinetics of roughening interfaces via incorporating surface tension and elastic and

viscous effects [54].

In the meantime, the temperature is a key parameter, the effect of which has proven to be instrumental in the experimental surface film growth [55], as well as in the molecular dynamics simulations of  $Li^+$  diffusional transport in the SEI (i.e. 250–400K) [56]. More specifically, temperature has been explored to shape the surface morphology and dendrite formation of microstructures [57, 58, 59]. It has been shown that the elevated temperatures (i.e.  $60^\circ - 80^\circ$ ) transform the SEI layer into a uniform compact layer which can delay the instigation of dendrites [60, 61]. However, later on, lowering the system temperature increases the diffusion resistance and decreases the surface film thickness which is favorable for suppressing the dendrites [62, 63].

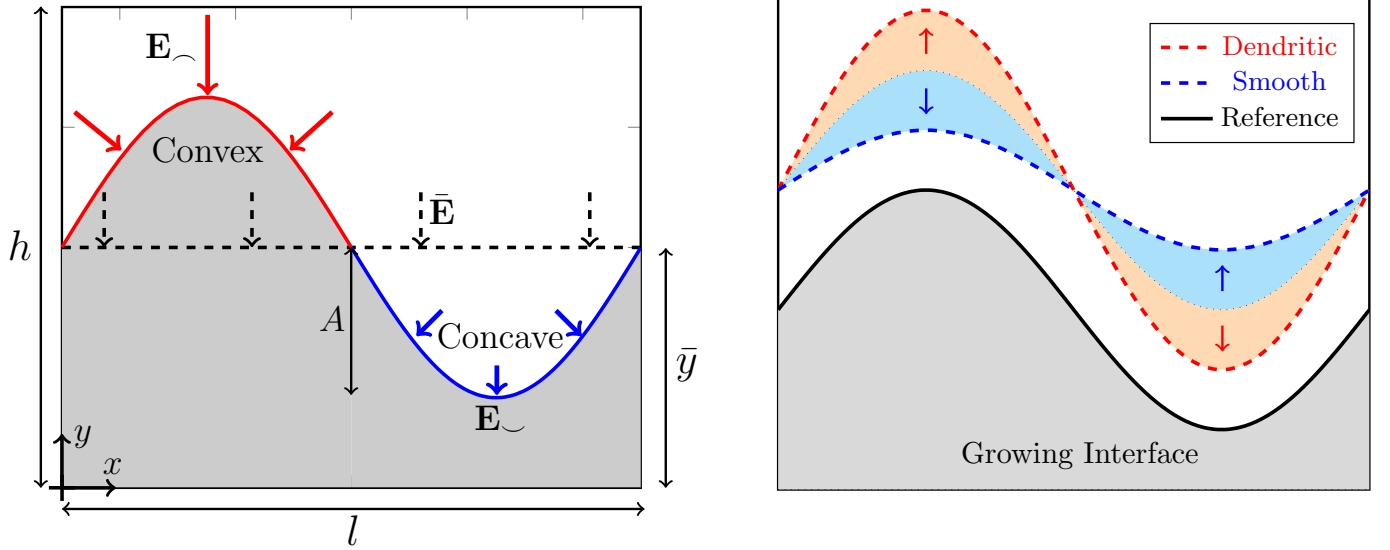
While the presence of surface roughness, consisting of the convex (i.e. peak) and concave (i.e. valley) regions, favors the electrodeposition in the convex zones, in this paper we counter such effect via imposing a temperature field in the opposite direction, which forms a bias for favoring the electrodeposition in the concave (i.e. valleys) sites. Obtaining the voltage  $V$  and temperature field  $T$ , we characterize the space of physical parameters for the efficacy of the imposed temperature gradient. The obtained framework could be useful for controlling the growing dendrites in the electrochemical systems, particularly those consuming larger power, where the microstructures could grow with runaway behavior.

## 2 Methodology

From the atomic perspective, dendritic propagation and formation of rough interfaces are inevitable, and fast processes occur under non-equilibrium conditions. Such a kinetics-dominated event rapidly accumulates the ions with random walks (i.e., Brownian dynamics), which is distinguishable from typical thermodynamics-dominated bonding under slow, close-to-equilibrium conditions.

From the continuum perspective, the development of the interfacial morphology depends on the macro-scale electrochemical parameters which include the electric field and electrolyte diffusivity. Such variables control the accessibility of ions to the electrodeposition sites and the rate of interface growth.

As shown in Figure 1a, such stochastic interactions should yield a fast-growing asperity (i.e. convex:  $\frown$ ), followed by a slow-growing hollow region (i.e. concave:  $\smile$ ). The difference in the growth rate is due to the peaks having better proximity for the upcoming ions as well as possessing geometry-induced



(a) Surface heterogeneity model, respectively. Black dashed arrows illustrate the average electric field for the equivalent flat geometry.  $h, l$ : domain height and length,  $\bar{y}$ : average elevation of interface,  $x, y$ : coordinates.

(b) The illustration of evolution dynamics, where the reference interface (i.e. black) can either grow stable (i.e. blue) or unstable (i.e. red). In stable growth, the convex (top) and concave (bottom) regions get closer to each other (blue arrows), while during unstable growth they get further away from each other (red arrows).

Figure 1: The convex and concave regions in the perturbed interface are compared in terms of (a) Electric field, and (b) Growth stability.

higher directed electric field ( $\mathbf{E}_{\text{convex}} > \mathbf{E}_{\text{concave}}$ ). Hence the evolved microstructures will acquire a certain roughness, which grows with runaway behavior [29, 64]. Therefore, we aim to counter such instability by imposing a reaction-rate bias in favor of the concave region, which is controlled by the temperature field  $T$ .

CX, CV

## 2.1 Electric Field

The perturbation in the growing interface can be modeled in a sinusoidal form, where concave (i.e. valley:  $\cup$ ) and convex (i.e. peak:  $\cap$ ) regions are connected as shown in the Figure 1b. The elevation of the interfacial roughness  $y_I$  could be expressed in terms of the horizontal variable  $x$  as:

$$y_I = \bar{y} + A \sin\left(\frac{2\pi\omega x}{l}\right) \quad (1)$$

where  $\bar{y}$  is the average elevation of the growing microstructure,  $A$  is the amplitude of the perturbation,

$\omega$  is the frequency of the repetition, and  $l$  is the domain length. Thus, the maximum curvature  $\kappa$  occurs in the peaks and valleys ( $|\sin(\dots)| = 1 \rightarrow x = \pm \frac{l}{4\omega}$ ) as :

$$\kappa = \frac{y_I''}{\sqrt{(1 + y_I'^2)^3}} \Big|_{x = \frac{l}{4\omega}} = -A \left( \frac{2\pi\omega}{l} \right)^2 \quad (2)$$

Therefore, one can calculate the ratio of the maximum-to-minimum electric field  $\hat{E} := \frac{E_{\frown}}{E_{\smile}}$ , which is a measure of how critically the roughening interface. In this regard, the maximum and minimum electric field, depend on both the radius of curvature  $r$  (i.e.  $r = \frac{1}{\kappa}$ ), the applied voltage of  $V_+$  and  $V_-$  between two electrodes as well as the remaining distance of the interface from the counter electrode (i.e.  $h - y_I$ ). Thus the electric field in any position can be described as:

$$E = f(r) \frac{V_+ - V_-}{h - y_I} \quad (3)$$

where  $f(r)$  is the curvature dependents augmentation (or diminishing) factor based on the interface geometry. Particularly for the ratio of the electric field  $\hat{E}$  between the convex  $E_{\frown}$  and concave  $E_{\smile}$  surfaces (i.e.  $\hat{E} = E_{\frown}/E_{\smile}$ ) is obtained as:

$$\hat{E} = \frac{f_{max}(\hat{r})}{f_{min}(\hat{r})} \frac{h - y_{min}}{h - y_{max}}$$

where  $y_{min}$  and  $y_{max}$  are the respective elevations at concave and convex surfaces and  $\hat{r} := \frac{r}{h}$  is the normalized radius of curvature. In fact for the convex interface, the electric field is augmented ( $f_{max}(\hat{r}) > 1$ ), and vice versa for the concave interface it gets diminished ( $f_{min}(\hat{r}) < 1$ ). Hence, in terms of the curvature effect, one gets the following order:

$$E_{\frown} > \bar{E} > E_{\smile} \quad (4)$$

where the indexes  $\square_{\frown}$ ,  $\bar{\square}$ , and  $\square_{\smile}$  represent the convex (i.e. peak), flat, and concave (i.e. valley) regions respectively.

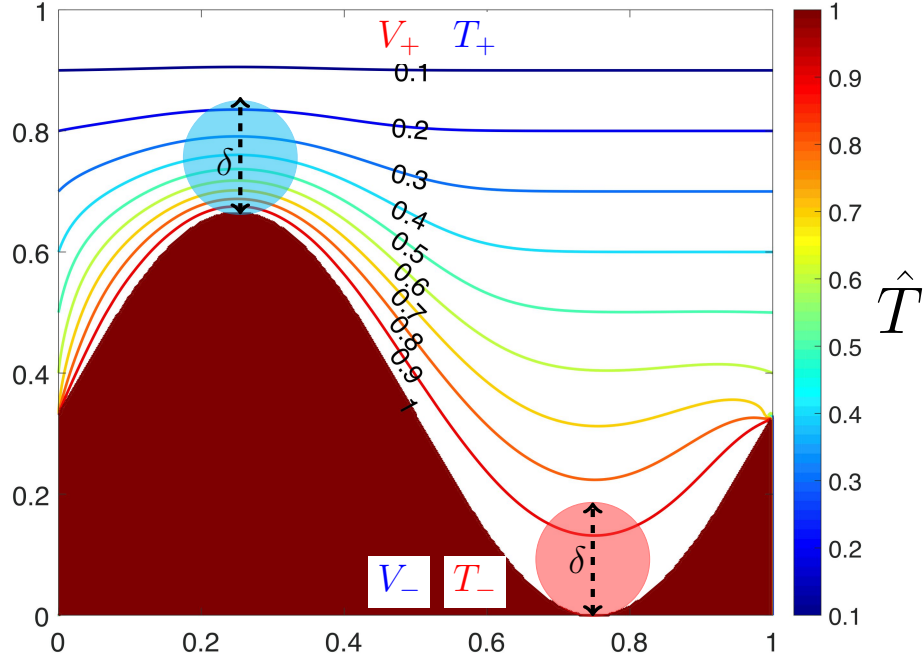


Figure 2: The temperature map for the roughened surface is characterized by convex (*peaks*) and concave (*valleys*) regions. Lines show the dimension-less temperature map (i.e.  $\hat{T} = \frac{T - T_+}{T_- - T_+}$ ), with the bottom (i.e.  $T_-$ ) and top (i.e.  $T_+$ ) electrodes temperatures. The growing interface remains isothermal with the connected electrode (i.e.  $T_-$ ). The temperature distribution is obtained later in the section 3.

## 2.2 Temperature Gradient

The temperature has a deterministic role in the rate of the electrodepositing reactions, which is generally expressed via the Arrhenius relationship. The diffusivity of the ions  $D$  within the electrolyte is governed by the following relationship [65]:

$$D = D_0 \exp\left(-\frac{Q}{k_B T}\right) \quad (5)$$

where  $D_0$  is a pre-factor and the  $Q$  is activation energy for the diffusivity and  $k_B$  is the Boltzmann's constant. Figure 2 illustrates a sample of a formed temperature field in the vicinity of the convex (blue circle) and concave (red) sites when a higher temperature is imposed in the negative electrode ( $T_- > T_+$ ). Since the concave region is surrounded by higher temperature interface it will get a higher temperature. Conversely, the sticking-out convex peak will have less of the higher temperature interface in its surroundings and hence gets lower temperature values. Consequently, the concave regions possess warmer electrolytes than their convex counterpart. In this context, while the electric field, forms a bias

Variable	$D$	$C_0$	$l$	$R$	$T$	$V_0$	$z$	$F$
Value	$2.3 \times 10^{-10}$	$10^3$	25	8.3	298	3.6	1	96.4
Unit	$m^2.s^{-1}$	$mol.m^{-3}$	$\mu m$	$J.mol^{-1}.K^{-1}$	$K$	$V$	[ ]	$kC.mol^{-1}$
Ref.	[67]	Assumed	[68]	[69]	Ambient	[70]	for $Li^+$ [71]	[69]

Table 1: Physical parameters.

for more growth in the convex region, imposing the higher temperature at the negative electrode could cause a countering bias for more electrodeposition in the concave sites. This could be explained in terms of the ionic flux  $J$ , which is described as [66]<sup>2</sup>:

$$J = -D\nabla C - \frac{zF}{RT}DC\nabla V \quad (6)$$

where  $D$  is the diffusivity of the ions in the electrolytic medium,  $C$  is the local concentration of the electrolyte,  $z$  is the valence number of the charge carriers,  $F$  is the Faraday's constant,  $R$  is the gas constant,  $T$  is the local temperature and  $V$  is the local voltage. Therefore, while the electric field  $E$ , as a non-material-independent property, favors higher flux in the convex interface, the diffusivity as a material-dependent property could favor higher ionic flux at the concave sites and balance out the electrodeposition for forming more uniform interface, and one gets:

$$D_{\curvearrowright} > \bar{D} > D_{\curvearrowleft} \quad (7)$$

which tends to counter the the electric field effect obtained earlier in the Equation 4.

## 2.3 Stability Condition

The comparative scale of the convex and concave zones, illustrated in Figure 2 falls in the continuum realms, which extends significantly larger than the smaller-scale electrodeposition sites in the interface (i.e. Helmholtz layer, double layer, space-charge, etc). Such a large-scale zone is in electro-neutral condition [72], where the continuum relationship for ionic flux is in effect. In fact, the ionic flux (Equation 6) is composed of mainly-diffusion ( $D\nabla C$ ) and electro-migration ( $\frac{zF}{RT}DC\nabla V$ ). Herein we compare these two terms using the typical value in the Table 1, as below:

---

<sup>2</sup>In the absence of convection.

$$\begin{cases} J_{\text{Diff}} = D\nabla C \sim \frac{2DC_0}{l} \sim 10^{-2} \frac{\text{mol}}{\text{m}^2 \cdot \text{s}} & \text{Diffusion} \\ J_{\text{Mig}} = \frac{zF}{RT} DC \nabla V \sim \frac{De}{k_B T} zFC_0 \frac{V_0}{l} \sim 1 \frac{\text{mol}}{\text{m}^2 \cdot \text{s}} & \text{Electro-migration} \end{cases}$$

which means that for the typical value  $J_{\text{Mig}} \gg J_{\text{Diff}}$  ; not to mention that for the voltage  $V$ , the effective zone of variation is the space-charge region (i.e.  $x_I$ ) [72] which would make  $J_{\text{Mig}}$  even larger. In fact, the migration efficacy for ionic flux occurs when the applied voltage is high enough. In such conditions, the drift velocity  $v_d$  of the charge carriers will be effective, which feeds the electrodeposition sites and determines the rate of interface growth, and is defined as [71]:

$$v_d = \mu \mathbf{E} \quad (8)$$

where  $\mu$  and  $\mathbf{E}$  are the local ionic mobility and electric field respectively. As well considering the correlation of the electrical mobility  $\mu$  with the diffusivity  $D$  (ie. Einstein relationship where  $\mu \sim \frac{D}{T}$ ), one would require faster electrodeposition in the concave zone and the convex counterpart for achieving stability (i.e.  $v_{d,\smile} > v_{d,\frown}$ ). Hence assuming similar grown porosity in the convex and concave zones one gets:

$$\frac{D_{\smile} E_{\smile}}{T_{\smile}} > \frac{D_{\frown} E_{\frown}}{T_{\frown}} \quad (9)$$

where considering the correlation of the diffusivity  $D$  with the temperature  $T$  (Equation 5) one achieves:

$$\frac{T_{\frown}}{T_{\smile}} \exp\left(\frac{Q}{k_B} \left(\frac{1}{T_{\frown}} - \frac{1}{T_{\smile}}\right)\right) > \frac{E_{\frown}}{E_{\smile}} \quad (10)$$

and the required activation energy of the electrolyte  $Q$ , such that the concave zone ( $\smile$ ) could catch up with the convex zone ( $\frown$ ) is obtained as:

$$\boxed{Q > \frac{T_{\smile} T_{\frown}}{T_{\smile} - T_{\frown}} k_B \ln\left(\frac{E_{\frown} T_{\smile}}{E_{\smile} T_{\frown}}\right)} \quad (11)$$

which provides the stability criterion for the stable evolution of the interfacial perturbation when the temperature gradient is imposed.



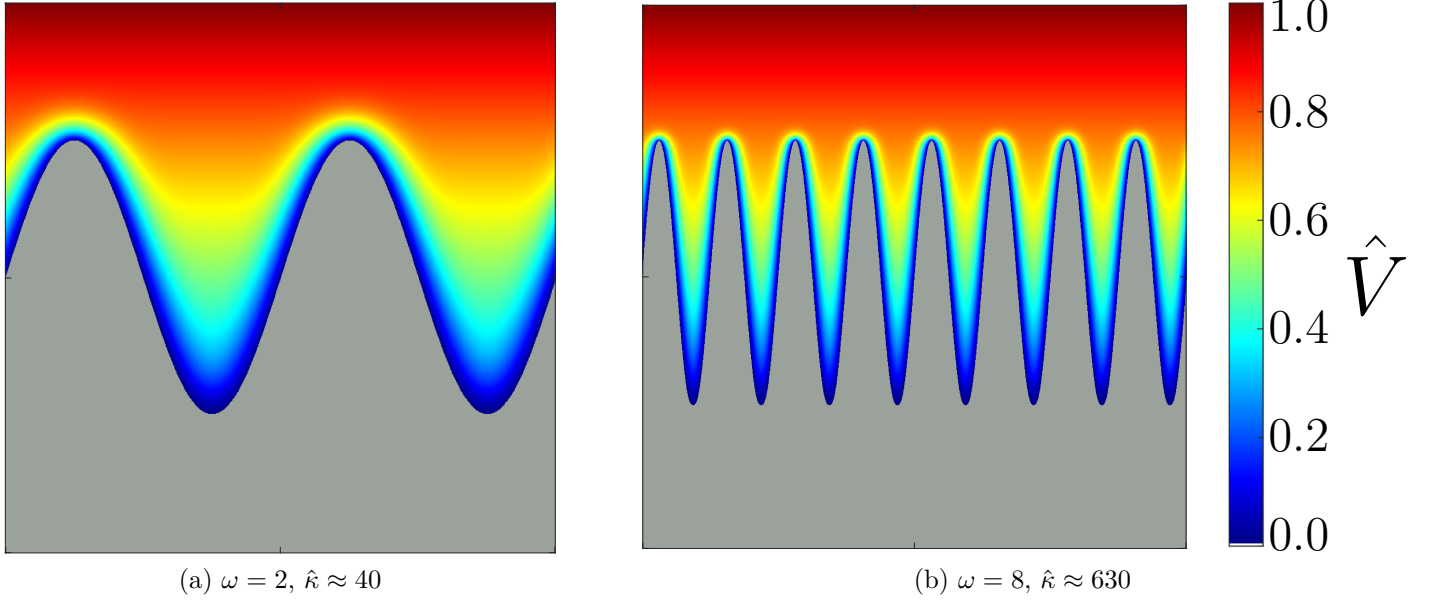


Figure 3: The distribution in the normalized voltage  $\hat{V}$  for various normalized curvatures  $\hat{\kappa}$ . Gray area represents the growing (i.e. dendritic) interface.

### 3 Numerical Computation

#### 3.1 Voltage distribution $V$

In order to calculate the maximum  $E_{\perp}$  and minimum  $E_{\parallel}$  electric fields, one needs to compute the voltage distribution, in the vicinity of these sites. In this regard, Poisson's Equation could describe the continuum voltage mapping, given as [73]:

$$\nabla^2 V = \frac{\rho}{\epsilon} \quad (12)$$

where  $\rho$  is the local charge density and  $\epsilon$  is the permittivity of the electrolyte medium. Due to the large scale of the interface perturbation ( $\sim \mu m$ ), a fair assumption is that a significant portion of the medium falls out of the double layer region ( $\sim nm$ ). Therefore, a simplified version of the Equation 12 for the voltage distribution in 2D would be [74]:

$$\frac{\partial^2 V}{\partial x^2} + \frac{\partial^2 V}{\partial y^2} \approx 0 \quad (13)$$

Therefore the domain could get partitioned into a 2D grid of  $n_x \times n_y$  points where  $n_x$  and  $n_y$  are the number of grid points in  $x$  and  $y$  directions respectively. Which are selected large enough to be able to

capture the voltage variations in the convex ( $\smile$ ) and concave ( $\frown$ ) sites.

Hence  $V_{i,j}$  represents the voltage at the node  $x_j$  and  $y_i$ . Performing a finite difference scheme on the equation 13, one has:

$$\frac{(V_{i,j+1} - 2V_{i,j} + V_{i,j-1}))}{\delta x^2} + \frac{V_{i+1,j} - 2V_{i,j} + V_{i-1,j}}{\delta y^2} \approx 0 \quad (14)$$

re-arrangement gives:

$$V_{i,j} \approx \frac{V_{i+1,j} + V_{i-1,j} + \frac{\delta y^2}{\delta x^2} (V_{i,j+1} + V_{i,j-1}))}{2 \left( 1 + \frac{\delta y^2}{\delta x^2} \right)} \quad (15)$$

Regarding the boundary conditions, from Figure 1a, since the metallic interface is physically connected to the negative pole, one has:

$$\begin{cases} V(x, 0) = V_- \\ V = V_- & y \leq y_I \\ V(x, h) = V_+ \end{cases} \quad (16)$$

which are the Dirichlet boundary conditions for the discretized equation 15, and  $V_-$  and  $V_+$  are the voltage values for the negative electrode and the positive electrode.

The initial voltage value  $V_0$  is set as the uniform distribution in the domain between the negative and positive electrode, except the interface which is physically touching the negative electrode ( $V_-$ ) as:

$$V_0(x, y) = \begin{cases} V_- & y \leq y_I \\ V_- + \left( \frac{V_+ - V_-}{h} \right) y & y > y_I \end{cases} \quad (17)$$

Subsequently, the voltage of the grid points  $V_{i,j}$  was updated from the neighboring grid points (top  $\uparrow$ , bottom  $\downarrow$ , left  $\leftarrow$ , and right  $\rightarrow$ ), through the successive steps based on the equation 15. During each iteration, the boundary conditions, in the Equation 16 were enforced from the electrodes and the interfaces. As well, regarding the left/right boundaries the periodic boundary condition (*PBC*) was applied, which indicates that the voltage values between the left/right boundaries are transferred to each other.

Throughout the successive runs, the convergence criterion is defined by a maximum difference of the voltage values  $V_{i,j}$  varying of next iteration  $(k + 1)$  from the previous one  $(k)$ , which is tracked as the error. The iterations were stopped when the error value got smaller (or equal) to the assigned threshold value. Figure 3 visualizes the converged final voltage distribution for both low- and high-curvature perturbations.

Finally, the average electric field across the highlighted regions of the convex (i.e.  $E_{\curvearrowright}$ ) and concave (i.e.  $E_{\curvearrowleft}$ ) regions in the Figure 2 are calculated via approximating  $E = -\nabla V$  as:

$$E \approx \frac{V_{\text{Top}} - V_{\text{Bot}}}{\delta} \quad (18)$$

where  $V_{\text{Top}}$  and  $V_{\text{Bot}}$  are the converged voltage values in the top and bottom ends of the focused zones in both convex ( $\curvearrowright$ ) and concave ( $\curvearrowleft$ ) zones and  $\delta$  is their respective diameter.

### 3.2 Temperature distribution $T$

The relationship for transition and dispersal of the temperature is expressed as[75]:

$$\frac{\partial T}{\partial t} = \alpha \left( \frac{\partial^2 T}{\partial x^2} + \frac{\partial^2 T}{\partial y^2} \right) \quad (19)$$

since the rate of growth in the moving boundary  $\frac{\partial y_I}{\partial t}$  is far less than the dynamics of the convergence of the temperature  $\frac{\partial T}{\partial t}$  ( $\frac{\partial y_I}{\partial t} \ll \frac{\partial T}{\partial t}$ ), during the growth process the boundary could get assumed as quasi-stationary with respect to the transition of the temperature field, which means that the temperature profile can be treated as the quasi-steady state  $\frac{\partial T}{\partial t} \approx 0$ , and the temperature profile is given via:

$$\frac{\partial^2 T}{\partial x^2} + \frac{\partial^2 T}{\partial y^2} \approx 0 \quad (20)$$

regarding the boundary conditions, the temperature values are constant in the electrodes after applying the temperature gradient ( $T_- > T_+$ ). As well, since the thermal diffusivity of the growing metallic interface  $\alpha_I$  is significantly larger than the non-metallic metallic boundary  $\alpha_{El}$  ( $\alpha_I \gg \alpha_{El}$ ), the rate of temperature variation will also be significantly larger and it remains relatively isothermal with the electrode (i.e.  $T_-$ ). This means that the interface temperature could be assumed as the quasi-steady

state compared to the electrolytic domain, and the temperature boundary condition will be established as:

$$\begin{cases} T(x, 0) = T_- \\ T = T_- & y \leq y_I \\ T(x, h) = T_+ \end{cases} \quad (21)$$

It is noticeable that the relationships and boundary conditions for the temperature in the Equations 20 and 21 are similar to the relationships for the voltage distribution in the Equations 13 and 16. Hence one can avoid repeated computations by projecting the temperature profile  $T$  from the voltage profile  $V$ . In this regard, we define the dimension-less parameters for the voltage  $\hat{V}$  and temperature  $\hat{T}$  as:

$$\begin{cases} \hat{V} = \frac{V - V_-}{V_+ - V_-} & 0 \leq \hat{V} \leq 1 \\ \hat{T} = \frac{T - T_+}{T_- - T_+} & 0 \leq \hat{T} \leq 1 \end{cases}$$

Noting that the gradient of the temperature field is imposed as opposite to the voltage field, the temperature field is obtained as:

$$\hat{T} = 1 - \hat{V} \quad (22)$$

Figures 4a and 4b illustrate the variation of the temperature versus the normalized vertical distance above the convex (i.e. peak) and concave (i.e. valley) sites ( $\hat{y} - \hat{y}_I$ ) respectively. Here, one can infer the effect of the curved boundary on the temperature profile as:

$$\left. \frac{\partial^2 T}{\partial \hat{y}^2} \right|_{\curvearrowleft} < 0, \quad \left. \frac{\partial^2 T}{\partial \hat{y}^2} \right|_{\curvearrowright} > 0$$

which means that the average temperature in the convex  $\bar{T}_{\curvearrowleft}$  and concave  $\bar{T}_{\curvearrowright}$  sites (blue and red circles in the Figure 2) differ considerably, which can be obtained via integrating in the region as:

$$\bar{T} = \frac{1}{\hat{\delta}} \int_0^{\hat{\delta}} T dy$$

and one gets:

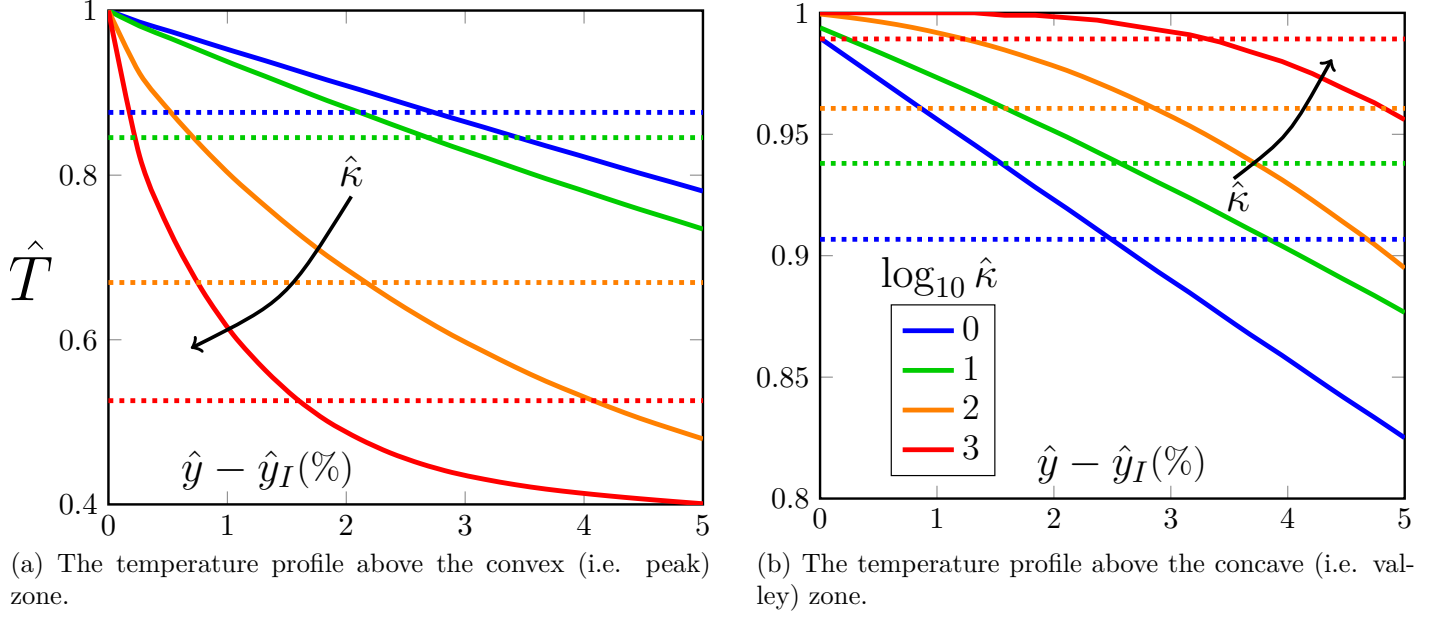


Figure 4: The normalized temperature profile  $\hat{T}$  versus the normalized vertical distance  $\hat{y} - \hat{y}_I$ , above (a) the convex (i.e. peak) and (b) the concave (i.e. valley) regions for various normalized curvature values  $\hat{\kappa}$ .

$$\bar{T}_{\smile} > \bar{T}_{\frown} \quad (23)$$

which are shown as dashed lines in these two Figures.

## 4 Results & Discussions

### 4.1 Stability Analysis

The temperature difference, given in the Equation 23 provides the possibility for higher diffusion of the ions in the concave ( $\frown$ ) sites relative to the convex ( $\smile$ ) counterpart regions. One effective parameter for the imposed temperature gradient  $\Delta T$  is the sensitivity of the resulted diffusivity  $D$ , which can be obtained as:

$$\frac{\partial D}{\partial T} = -\frac{Q}{k_B T} D$$

Here it is evident that one effective parameter for such sensitivity is the activation energy  $Q$ . In other words, for an electrolyte more responsive to the temperature (i.e.  $Q \uparrow$ ), less temperature is needed

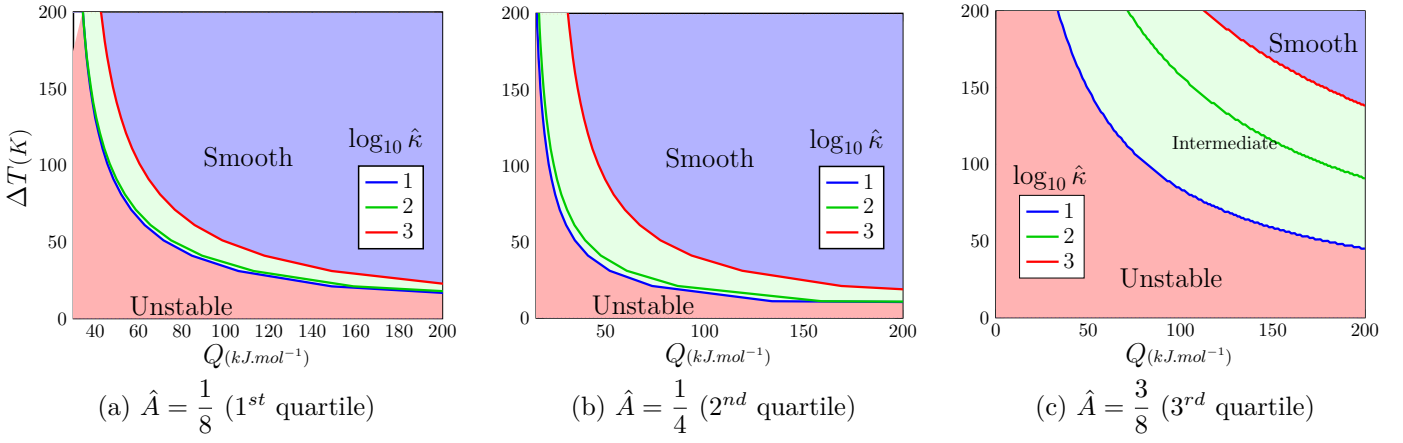


Figure 5: Visualized zones of the required temperature difference  $\Delta T$  versus the activation energy  $Q$ , for half-way progress of the interface (i.e.  $\bar{y} = \frac{h}{2}$ ) for the three-quarters of the destabilized growth ( $\hat{A} = \left\{\frac{1}{4}, \frac{1}{2}, \frac{3}{4}\right\}$ ). The stable zones (blue) signify diffusion domination, and vice versa, the unstable zones (red) illustrate electromigration domination.

( $\Delta T \downarrow$ ) to form stable growth. Considering the halfway progress of the interface ( $\bar{y} = \frac{h}{2}$ ), Figures 5a, 5b, and 5c visualize the range of required temperature gradient  $\Delta T$  versus the diffusion activation energy  $Q$  of the electrolyte, for three quartiles of destabilization  $\hat{A} = \left\{\frac{1}{4}, \frac{1}{2}, \frac{3}{4}\right\} \frac{h}{2}$ , which is additionally characterized in terms of interface curvature  $\hat{\kappa} = \kappa/h$ .

In this regard, the earlier slower growth of the stable zone (i.e.  $\hat{A} = \left\{\frac{1}{4} \rightarrow \frac{1}{2}\right\} \frac{h}{2}$ ) and its later fast diminishing (i.e.  $\hat{A} = \left\{\frac{1}{2} \rightarrow \frac{3}{4}\right\} \frac{h}{2}$ ) could get explained via the non-linear overall effect of the electric field  $E$  versus the temperature field  $T$  (Equation 10). Labeling the temperature and electric field roles as  $f_T := \frac{T_-}{T_+} \exp\left(\frac{Q}{k_B} \left(\frac{1}{T_-} - \frac{1}{T_+}\right)\right)$  and  $f_E := \frac{E_-}{E_+}$  respectively, the stable growth could get obtained when  $f_T > f_E$ . Therefore, during the earlier transition from 1<sup>st</sup> to 2<sup>nd</sup> quartile, it is obvious from the Equation 11 that while the competitive ratios of  $\frac{E_-}{E_+}$  and  $\frac{T_-}{T_+}$  carry smaller weight in the logarithm term, the primary impact is derived from the temperature difference, as:

$$Q > \sim \frac{1}{T_- - T_+}$$

In this regard, since the dimension-less voltage  $\hat{V}$  and temperature  $\hat{T}$  fields have been found to be complementary of each other in the Equation 22, one could ascribe the following correlation:

$$\hat{T} = 1 - \int_0^\delta \hat{E} dy$$

which means that the temperature field would be averaging the values across the focus region of scale  $\delta$  (Figure 2). In this regard, while considering solely the temperature ratio  $T_{\frown}/T_{\smile}$  between the concave and convex sites would carry a smaller effect than the electric field ratio  $\hat{E}$ , the exponential term  $\exp\left(\frac{Q}{k_B}\left(\frac{1}{T_{\frown}} - \frac{1}{T_{\smile}}\right)\right)$  empowers overall temperature effect  $f_T$ , which makes it dominate ultimately.

However, during the later-on transition from  $2^{nd}$  to  $3^{rd}$  quartile, since the difference in the remaining gap between the convex and concave sites grows rapidly, the overall electric field effect accelerates further and the required temperature gradient needs to be much higher. Such destabilizing trend is additionally observed versus the curvature increase in all these figures.

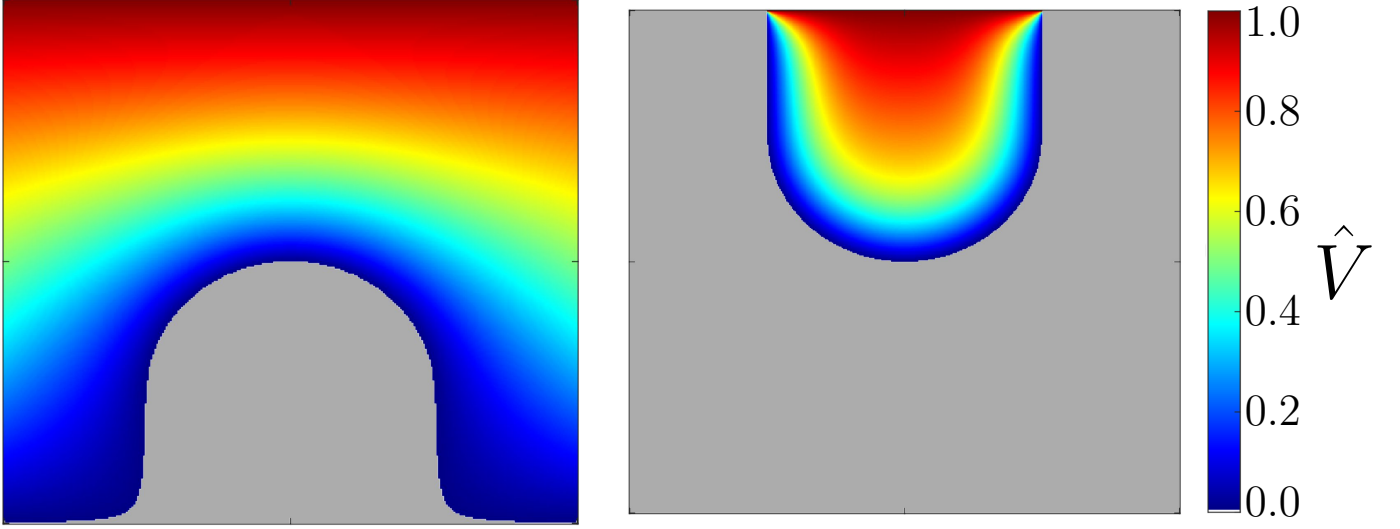
## 4.2 Curvature effect formulation

While the role of the curvature  $f(\hat{r})$  has been qualitatively explored in the previous sections, such augmentation/diminishing coefficient for convex/concave zone could get addressed quantitatively. In this regard, the Equation 3 can get normalized as:

$$\hat{E} = \frac{f(\hat{r})}{1 - \hat{y}_I}$$

where  $\hat{y}_I = \frac{y_I}{h}$  is the normalized average interface elevation. Considering a single semicircle with the prescribed normalized radius of curvature  $\hat{r} = r/h$ , set in the center of the domain, one could re-calculate the voltage field, repeating the procedure in the Section 3. Figures 6a and 6b, illustrate the resulting voltage distributions for convex and concave interface respectively.

From the Figure 6a, the augmentation coefficient  $f_{max}$  of the electric field in the convex sites due to radius of curvature, could be formulated. As the initial step, the limits can be placed, where for the minimal radius of curvature this radius gets indefinitely large, and vice versa for the very large radius of curvature it becomes ineffective. Hence:



(a) Normalized voltage map surrounding a convex region of the prescribed radius of curvature  $\hat{r} = 1/4$ , which augments the electric field on its high peak and is addressed by  $f_{max}$ .

(b) Normalized voltage map surrounding a concave region of the prescribed radius of curvature  $\hat{r} = 1/4$ , which diminishes the electric field on its bottom valley and is addressed by  $f_{min}$ .

Figure 6: Voltage distribution on the vicinity of a single (a) peak and (b) valley prescribed radius of curvature (i.e.  $\hat{r} = \frac{1}{\kappa}$ ), set in the center of the domain ( $y_I = \frac{h}{2}$ ). The grey region represents the grown interface (i.e.  $V = V_-$ ).

$$\begin{cases} \lim_{\hat{r} \rightarrow 0} f_{max} = \infty \\ \lim_{\hat{r} \rightarrow \infty} f_{max} = 1 \end{cases}$$

Therefore one could assign an interpolating function satisfying these boundary conditions, as below:

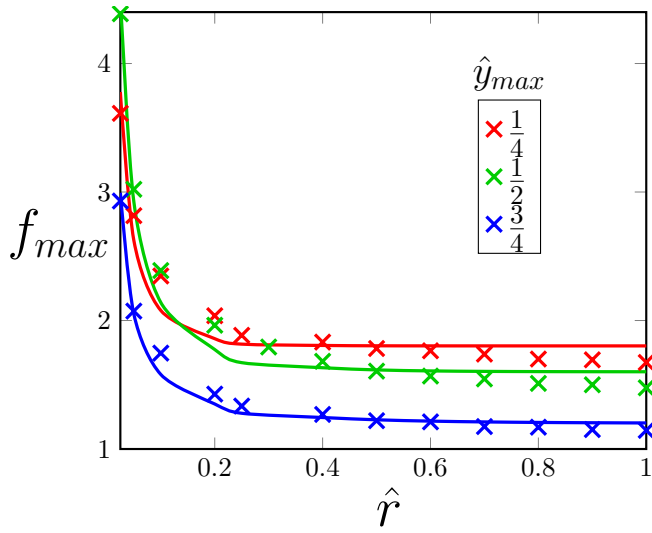
$$f_{max} = \frac{\exp(\alpha_1 \hat{r}) + \beta_1}{\exp(\alpha_1 \hat{r}) - 1} \quad (24)$$

where  $\alpha_1$  and  $\beta_1$  are the relaxation coefficients. Similarly, for Figure 6b, the diminishing coefficient  $f_{min}$  of the electric field in the concave regions due to the radius of curvature could be interpolated. In this regard, for the minimal radius of curvature, this coefficient gets indefinitely small, and vice versa for a very large radius of curvature it yields to unity (i.e. becomes ineffective). Hence:

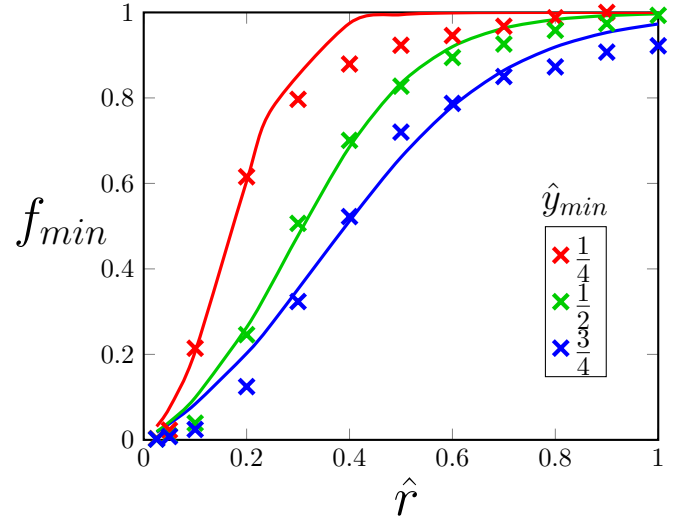
$$\begin{cases} \lim_{\hat{r} \rightarrow 0} f_{min} = 0 \\ \lim_{\hat{r} \rightarrow \infty} f_{min} = 1 \end{cases}$$

and one can define an interpolating function form to satisfy the above boundary condition as:





(a) Tracking the variation of the augmentation ratio  $f_{max}$  with respect to the radius of curvature  $\hat{r}$  in the convex interface for various interface height  $\hat{y}_{max}$ .  $\times$ : numerical computations, solid: interpolation via Equation 24.



(b) Tracking the variation of diminishing ratio  $f_{min}$  with respect to the radius of curvature  $\hat{r}$  in the concave interface for various average interface height  $\hat{y}_{min}$ .  $\times$ : numerical computations, solid: interpolation via Equation 25.

Figure 7: (a) The augmentation coefficient  $f_{max}$  (b) the diminishing coefficient  $f_{min}$ , versus normalized curvature of the interface  $\hat{r}$  for 3 quartile stages of the interface growth as  $\hat{y}_I := \left\{ \frac{1}{8}, \frac{2}{8}, \frac{3}{8} \right\}$ .

$$f_{min} = \frac{\exp(\alpha_2 \hat{r}) - 1}{\exp(\alpha_2 \hat{r}) + \beta_2} \quad (25)$$

where  $\alpha_2$  and  $\beta_2$  are the relaxation coefficients. For either augmentation or diminishing ratios the coefficients of  $\alpha_i$  and  $\beta_i$  are obtained via minimizing the sum of the squares of the errors from the computational values  $\hat{E}$  in the locus of  $y_{max}$  and  $y_{min}$  as:

$$\begin{aligned} & \forall \alpha_i, \beta_i \in \mathbb{R} && \text{Minimize Err} \\ \text{Such that} & \text{Err} = \sum_{k=1}^n \left| \frac{f_k}{1 - \hat{\lambda}_k} - \hat{E}_k \right|^2 \end{aligned}$$

where  $n$  is the number of points from the numerical computations <sup>3</sup>.

---

<sup>3</sup>Also obtainable using non-linear fit function in MATLAB ( i.e. *nlinfit* )

## 5 Conclusion

In this paper, we have developed an analytical/computational framework on the roughened growing interface, which is destabilized by the electric field bias, favoring the peaks (i.e. convex) over the valleys (i.e. concave). Imposing a countering temperature field in the electrodes, we establish a stability criterion for quantifying the space of required temperature gradient  $\Delta T$  versus the activation energy of diffusion  $Q$ , leading to the controlled interface growth. As well, we also formulate a curvature-dependent analytical approximation for augmentation/diminishing ratios for the electric field in the vicinity of the convex/concave interface. Such criterion establishes a relationship between the geometry of the interface, the physical properties of the electrolyte, and the operating conditions. The developed framework could be useful for designing the space of operational parameters for controlling the propagation of the microstructures and the prevention of runaway, during prolonged cycles, particularly when the surface roughness gets pronounced in the later stage of cycle life.

## Nomenclature

Symbol	Description	Symbol	Description
$\square_{\curvearrowright}$	Convex region property	$k_B$	Boltzmann's constant ( $J.K^{-1}.mol^{-1}$ )
$\square_{\curvearrowleft}$	Concave region property	$R$	Gas constant ( $J.mol^{-1}.K^{-1}$ )
$\mathbf{E}_{min}, \bar{\mathbf{E}}, \mathbf{E}_{max}$	min/average/max electric field ( $V.m^{-1}$ )	$D_0$	pre-exponential diffusivity ( $m^2.s^{-1}$ )
$l, h$	length/height of the domain ( $m$ )	$D$	Diffusion coefficient ( $m^2.s^{-1}$ )
$x, y$	horizontal/vertical coordinates	$\alpha_I, \alpha_{El}$	electrode/electrolyte thermal diff. ( $m^2.s^{-1}$ )
$y_I, \bar{y}$	local/average elevation of interface ( $m$ )	$T_+, T_-, \bar{T}$	top/bottom/average temperatures (K)
$A, \omega$	perturbation amplitude/freq. ( $m, []$ )	$V_+, V_-$	Cathode/Anode voltage (V)
$\kappa, r$	curvature/radius of curvature ( $m$ )	$\hat{T}, \hat{V}$	Normalized temperature/voltage
$C_0$	Bulk concentration ( $mol, m^{-3}$ )	$V_{Top}, V_{Bot}$	Voltages of the focus region (V)
$\epsilon$	Permittivity of the electrolyte ( $F.m^{-1}$ )	$y_{max}, y_{min}$	max/min location of the interface ( $m$ )
$\rho$	Local charge density ( $C.m^{-3}$ )	$f_{max}, f_{min}$	augmentation/diminishing coeff.s
$Q$	Diff. activation energy ( $kJ.mol^{-1}$ )	$\alpha_i, \beta_i$	Fitting relaxation coefficients
$z$	Valence number	$\delta$	Diameter of the focus region ( $m$ )

# Data Availability

The raw data for producing the results in this manuscript are freely available upon request from the corresponding author at [aryanfar@caltech.edu](mailto:aryanfar@caltech.edu).

## References

- [1] Peter J. Hall and Euan J. Bain. Energy-storage technologies and electricity generation. *Energy Policy*, 36(12):4352–4355, 2008.
- [2] Yuxing Wang, Bo Liu, Qiuyan Li, Samuel Cartmell, Seth Ferrara, Zhiquan Daniel Deng, and Jie Xiao. Lithium and lithium ion batteries for applications in microelectronic devices: A review. *Journal of Power Sources*, 286:330–345, 2015.
- [3] B. Kennedy, D. Patterson, and S. Camilleri. Use of lithium-ion batteries in electric vehicles. *Journal of Power Sources*, 90(2):156–162, 2000.
- [4] M Stanley Whittingham. History, evolution, and future status of energy storage. *Proceedings of the IEEE*, 100(Special Centennial Issue):1518–1534, 2012.
- [5] Peng Gu, Mingbo Zheng, Qunxing Zhao, Xiao Xiao, Huaiguo Xue, and Huan Pang. Rechargeable zinc–air batteries: a promising way to green energy. *Journal of Materials Chemistry A*, 5(17):7651–7666, 2017.
- [6] Noorden R Van. The rechargeable revolution: A better battery. *Nature*, 507(7490):26–28, 2014.
- [7] Alessandro Innocenti, Dominic Bresser, Jürgen Garche, and Stefano Passerini. A critical discussion of the current availability of lithium and zinc for use in batteries. *nature communications*, 15(1):4068, 2024.
- [8] Taehoon Kim, Wentao Song, Dae-Yong Son, Luis K Ono, and Yabing Qi. Lithium-ion batteries: outlook on present, future, and hybridized technologies. *Journal of materials chemistry A*, 7(7):2942–2964, 2019.
- [9] Jianhui Deng, Xiaoqing Yang, and Guoqing Zhang. Simulation study on internal short circuit of lithium ion battery caused by lithium dendrite. *Materials Today Communications*, 31:103570, 2022.

- [10] Siyuan Li, Jixiang Yang, and Yingying Lu. Lithium metal anode. *Encyclopedia of Inorganic and Bioinorganic Chemistry*, pages 1–21.
- [11] Genlan Rong, Xinyi Zhang, Wen Zhao, Yongcai Qiu, Meinan Liu, Fangmin Ye, Yan Xu, Jiafan Chen, Yuan Hou, Wanfei Li, et al. Liquid-phase electrochemical scanning electron microscopy for in situ investigation of lithium dendrite growth and dissolution. *Advanced Materials*, 29(13):1606187, 2017.
- [12] Kang Xu. Nonaqueous liquid electrolytes for lithium-based rechargeable batteries. *Chemical Reviews-Columbus*, 104(10):4303–4418, 2004.
- [13] Deepti Tewari, Sobana P Rangarajan, Perla B Balbuena, Yevgen Barsukov, and Partha P Mukherjee. Mesoscale anatomy of dead lithium formation. *The Journal of Physical Chemistry C*, 2020.
- [14] Jianan Wang, Shanshan Yi, Jianwei Liu, Shiyi Sun, Yunpeng Liu, Duowen Yang, Kai Xi, Guoxin Gao, Amr Abdelkader, Wei Yan, et al. Suppressing the shuttle effect and dendrite growth in lithium-sulfur batteries. *ACS nano*, 14(8):9819–9831, 2020.
- [15] Dingchang Lin, Yayuan Liu, and Yi Cui. Reviving the lithium metal anode for high-energy batteries. *Nature nanotechnology*, 12(3):194–206, 2017.
- [16] F. Orsini A.D. Pasquier B. Beaudoin J.M. Tarascon. In situ scanning electron microscopy (sem) observation of interfaces with plastic lithium batteries. *J. Power Sources*, 76:19–29, 1998.
- [17] C. Brissot, M. Rosso, J. N. Chazalviel, and S. Lascaud. Dendritic growth mechanisms in lithium/polymer cells. *J. Power Sources*, 81:925–929, 1999.
- [18] Hikaru Sano, Hikari Sakaebe, Hiroshi Senoh, and Hajime Matsumoto. Effect of current density on morphology of lithium electrodeposited in ionic liquid-based electrolytes. *Journal of The Electrochemical Society*, 161(9):A1236, 2014.
- [19] O. Crowther and A. C. West. Effect of electrolyte composition on lithium dendrite growth. *J. Electrochem. Soc.*, 155(11):A806–A811, 2008.
- [20] N. Schweikert, A. Hofmann, M. Schulz, M. Scheuermann, S. T. Boles, T. Hanemann, H. Hahn, and S. Indris. Suppressed lithium dendrite growth in lithium batteries using ionic liquid electrolytes:

- Investigation by electrochemical impedance spectroscopy, scanning electron microscopy, and in situ  $^7\text{Li}$  nuclear magnetic resonance spectroscopy. *J. Power Sources*, 228:237–243, 2013.
- [21] He Liu, Xin-Bing Cheng, Jia-Qi Huang, Hong Yuan, Yang Lu, Chong Yan, Gao-Long Zhu, Rui Xu, Chen-Zi Zhao, Li-Peng Hou, et al. Controlling dendrite growth in solid-state electrolytes. *ACS Energy Letters*, 5(3):833–843, 2020.
- [22] Shan Yan and Amy C Marschilok. Conversion-type electrodes for rechargeable lithium based batteries: Case studies of iron based conversion materials for lithium-ion batteries and molybdenum disulfides for lithium-sulfur batteries. 2022.
- [23] J. Steiger, D. Kramer, and R. Monig. Mechanisms of dendritic growth investigated by in situ light microscopy during electrodeposition and dissolution of lithium. *J. Power Sources*, 261:112–119, 2014.
- [24] Kishen Rafiz, Dheeraj Ram Lingam Murali, and Jerry YS Lin. Suppressing lithium dendrite growth on lithium-ion/metal batteries by a tortuously porous  $\gamma$ -alumina separator. *Electrochimica Acta*, 421:140478, 2022.
- [25] Indrajeet V Thorat, David E Stephenson, Nathan A Zacharias, Karim Zaghib, John N Harb, and Dean R Wheeler. Quantifying tortuosity in porous li-ion battery materials. *Journal of Power Sources*, 188(2):592–600, 2009.
- [26] Andrew Cannon and Emily M Ryan. Characterizing the microstructure of separators in lithium batteries and their effects on dendritic growth. *ACS Applied Energy Materials*, 4(8):7848–7861, 2021.
- [27] Christoffer P Nielsen and Henrik Bruus. Morphological instability during steady electrodeposition at overlimiting currents. *Physical Review E*, 92(5):052310, 2015.
- [28] Asghar Aryanfar, Ali Tayyar, and William A Goddard III. Dendritic propagation on circular electrodes: The impact of curvature on the packing density. *Physical Review E*, 108(1):014801, 2023.
- [29] Peng Bai, Ju Li, Fikile R Brushett, and Martin Z Bazant. Transition of lithium growth mechanisms in liquid electrolytes. *Energy & Environmental Science*, 9(10):3221–3229, 2016.

- [30] Chunhao Yuan, Wenquan Lu, and Jun Xu. Unlocking the electrochemical–mechanical coupling behaviors of dendrite growth and crack propagation in all-solid-state batteries. *Advanced Energy Materials*, 11(36):2101807, 2021.
- [31] C. Monroe and J. Newman. The effect of interfacial deformation on electrodeposition kinetics. *J. Electrochem. Soc.*, 151(6):A880–A886, 2004.
- [32] Daniel A Cogswell. Quantitative phase-field modeling of dendritic electrodeposition. *Physical Review E*, 92(1):011301, 2015.
- [33] Chih-Hung Chen and Chun-Wei Pao. Phase-field study of dendritic morphology in lithium metal batteries. *Journal of Power Sources*, 484:229203, 2021.
- [34] Aniruddha Jana, David R Ely, and R Edwin García. Dendrite-separator interactions in lithium-based batteries. *Journal of Power Sources*, 275:912–921, 2015.
- [35] Jaehyuk Choi, Darren Crowdy, and Martin Z Bazant. Diffusion-limited aggregation on curved surfaces. *Europhysics Letters*, 91(4):46005, 2010.
- [36] Asghar Aryanfar, Daniel Brooks, Boris V. Merinov, William A. Goddard Iii, AgustÃn J. Colussi, and Michael R. Hoffmann. Dynamics of lithium dendrite growth and inhibition: Pulse charging experiments and monte carlo calculations. *The Journal of Physical Chemistry Letters*, 5(10):1721–1726, 2014.
- [37] Asghar Aryanfar, Michael R Hoffmann, and William A Goddard III. Finite-pulse waves for efficient suppression of evolving mesoscale dendrites in rechargeable batteries. *Physical Review E*, 100(4):042801, 2019.
- [38] Alexandre M Tartakovsky, Paul Meakin, Timothy D Scheibe, and Rogene M Eichler West. Simulations of reactive transport and precipitation with smoothed particle hydrodynamics. *Journal of Computational Physics*, 222(2):654–672, 2007.
- [39] Andrew Cannon, James G McDaniel, and Emily Ryan. Smoothed particle hydrodynamics modeling of electrodeposition and dendritic growth under migration-and diffusion-controlled mass transport. *Journal of Electrochemical Energy Conversion and Storage*, 20(4):041006, 2023.

- [40] Christoffer P Nielsen and Henrik Bruus. Sharp-interface model of electrodeposition and ramified growth. *Physical Review E*, 92(4):042302, 2015.
- [41] Guangyu Liu and Wei Lu. A model of concurrent lithium dendrite growth, sei growth, sei penetration and regrowth. *Journal of The Electrochemical Society*, 164(9):A1826, 2017.
- [42] Tara Foroozan, Fernando A Soto, Vitaliy Yurkiv, Soroosh Sharifi-Asl, Ramasubramonian Deivanayagam, Zhennan Huang, Ramin Rojaee, Farzad Mashayek, Perla B Balbuena, and Reza Shahbazian-Yassar. Synergistic effect of graphene oxide for impeding the dendritic plating of li. *Advanced Functional Materials*, 28(15):1705917, 2018.
- [43] Longchao Cao, Dehao Liu, Ping Jiang, Xinyu Shao, Qi Zhou, and Yan Wang. Multi-physics simulation of dendritic growth in magnetic field assisted solidification. *International Journal of Heat and Mass Transfer*, 144:118673, 2019.
- [44] Domenic Cipollone, Hui Yang, Feng Yang, Joeseeph Bright, Botong Liu, Nicholas Winch, Nianqiang Wu, and Konstantinos A Sierros. 3d printing of an anode scaffold for lithium batteries guided by mixture design-based sequential learning. *Journal of Materials Processing Technology*, 295:117159, 2021.
- [45] Luwei Shi, Longxing Zhang, Yanping Yang, Haipeng Zhang, Ruijie Yao, Caoquan Yuan, and Shaobo Cheng. In situ nano-sio2 electrospun polyethylene-oxide-based nano-fiber composite solid polymer electrolyte for high-performance lithium-ion batteries. *Nanomaterials*, 13(7):1294, 2023.
- [46] PP Natsiavas, K Weinberg, D Rosato, and M Ortiz. Effect of prestress on the stability of electrode–electrolyte interfaces during charging in lithium batteries. *Journal of the Mechanics and Physics of Solids*, 95:92–111, 2016.
- [47] W. Li, H. A. Tchelepi, Y. Ju, and D. M. Tartakovsky. Stability-guided strategies to mitigate dendritic growth in lithium-metal batteries. *J. Electrochem. Soc.*, 169(6):060536, 2022.
- [48] Rohan Akolkar. Mathematical model of the dendritic growth during lithium electrodeposition. *J. Power Sources*, 232:23–28, 2013.
- [49] Mihir N Parekh, Christopher D Rahn, and Lynden A Archer. Controlling dendrite growth in lithium metal batteries through forced advection. *Journal of Power Sources*, 452:227760, 2020.

- [50] Meghann C Ma, Gaojin Li, Xinye Chen, Lynden A Archer, and Jiandi Wan. Suppression of dendrite growth by cross-flow in microfluidics. *Science advances*, 7(8):eabf6941, 2021.
- [51] Li Ting Gao and Zhan-Sheng Guo. Effects of optimized electrode surface roughness and solid electrolyte interphase on lithium dendrite growth. *Energy Technology*, 9(7):2000968, 2021.
- [52] Hyunjoo Lee, Taejin Kwak, Wooju Lee, Jongchan Song, and Dongchoul Kim. Effect of surface topography on dendritic growth in lithium metal batteries. *Journal of Power Sources*, 552:232264, 2022.
- [53] He Liu, Xin-Bing Cheng, Zhehui Jin, Rui Zhang, Guoxiu Wang, Long-Qing Chen, Quan-Bing Liu, Jia-Qi Huang, and Qiang Zhang. Recent advances in understanding dendrite growth on alkali metal anodes. *EnergyChem*, 1(1):100003, 2019.
- [54] Michel Armand. Polymer solid electrolytes-an overview. *Solid State Ionics*, 9:745–754, 1983.
- [55] A.N. Dey. Lithium anode film and organic and inorganic electrolyte batteries. *Thin Solid Films*, 43(1):131–171, 1977.
- [56] Hitoshi Ota, Xianming Wang, and Eiki Yasukawa. Characterization of lithium electrode in lithium imides/ethylene carbonate, and cyclic ether electrolytes: I. surface morphology and lithium cycling efficiency. *Journal of The Electrochemical Society*, 151(3):A427, 2004.
- [57] Ryo Mogi, Minoru Inaba, Yasutoshi Iriyama, Takeshi Abe, and Zempachi Ogumi. In situ atomic force microscopy study on lithium deposition on nickel substrates at elevated temperatures. *Journal of The Electrochemical Society*, 149(4):A385, 2002.
- [58] Asghar Aryanfar, Daniel J Brooks, Agust  n J Colussi, Boris V Merinov, William A Goddard III, and Michael R Hoffmann. Thermal relaxation of lithium dendrites. *Phys. Chem. Chem. Phys.*, 17(12):8000–8005, 2015.
- [59] Asghar Aryanfar, Tao Cheng, Agustin J Colussi, Boris V Merinov, William A Goddard III, and Michael R Hoffmann. Annealing kinetics of electrodeposited lithium dendrites. *The Journal of chemical physics*, 143(13):134701, 2015.



- [60] Adam Maraschky and Rohan Akolkar. Temperature dependence of dendritic lithium electrodeposition: a mechanistic study of the role of transport limitations within the sei. *Journal of The Electrochemical Society*, 167(6):062503, 2020.
- [61] A computational investigation of thermal effect on lithium dendrite growth. *Energy Conversion and Management*, 161:193–204, 2018.
- [62] R. Akolkar. Modeling dendrite growth during lithium electrodeposition at sub-ambient temperature. *J. Power Sources*, 246:84–89, 2014.
- [63] Corey T Love, Olga A Baturina, and Karen E Swider-Lyons. Observation of lithium dendrites at ambient temperature and below. *ECS Electrochemistry Letters*, 4(2):A24, 2015.
- [64] Asghar Aryanfar, Sajed Medlej, and William A Goddard III. Morphometry of dendritic materials in rechargeable batteries. *Journal of Power Sources*, 481:228914, 2021.
- [65] Keith J Laidler. The development of the arrhenius equation. *Journal of chemical Education*, 61(6):494, 1984.
- [66] Allen J Bard, Roger Parsons, and Joseph Jordan. *Standard potentials in aqueous solution*, volume 6. CRC press, 1985.
- [67] Robert A Noulty and Derek G Leaist. Diffusion in aqueous copper sulfate and copper sulfate-sulfuric acid solutions. *Journal of solution chemistry*, 16(10):813–825, 1987.
- [68] Jinhyeok Ahn, Minjae Kim, Junhyeok Seo, Sukeun Yoon, and Kuk Young Cho. Delineating the relationship between separator parameters and practical lithium metal batteries characteristics. *Journal of Power Sources*, 566:232931, 2023.
- [69] National Institute of Standards and Technology. NIST Physics Laboratory. *The NIST Reference on Constants, Units and Uncertainty*. National Institute of standards and technology, 1998.
- [70] Ji-Lei Shi, Dong-Dong Xiao, Mingyuan Ge, Xiqian Yu, Yong Chu, Xiaojing Huang, Xu-Dong Zhang, Ya-Xia Yin, Xiao-Qing Yang, Yu-Guo Guo, et al. High-capacity cathode material with high voltage for li-ion batteries. *Advanced Materials*, 30(9):1705575, 2018.

- [71] Allen J. Bard and Larry R. Faulkner. *Electrochemical methods: fundamentals and applications*. 2 New York: Wiley, 1980., 1980.
- [72] J. N. Chazalviel. Electrochemical aspects of the generation of ramified metallic electrodeposits. *Phys. Rev. A*, 42(12):7355–7367, 1990.
- [73] David J Griffiths. *Introduction to electrodynamics*. Cambridge University Press, 2023.
- [74] Ronald F Probstein. *Physicochemical hydrodynamics: an introduction*. John Wiley & Sons, 2005.
- [75] Theodore L Bergman, Theodore L Bergman, Frank P Incropera, David P Dewitt, and Adrienne S Lavine. *Fundamentals of heat and mass transfer*. John Wiley & Sons, 2011.